RESEARCH ARTICLE

NANO · MICRO small
www.small-journal.com

Tunable Magnetic Coupling in Graphene Nanoribbon Quantum Dots

Peter H. Jacobse, Mamun Sarker, Anshul Saxena, Percy Zahl, Ziyi Wang, Emma Berger, Narayana R. Aluru,* Alexander Sinitskii,* and Michael F. Crommie**

Carbon-based quantum dots (QDs) enable flexible manipulation of electronic behavior at the nanoscale, but controlling their magnetic properties requires atomically precise structural control. While magnetism is observed in organic molecules and graphene nanoribbons (GNRs), GNR precursors enabling bottom-up fabrication of QDs with various spin ground states have not yet been reported. Here the development of a new GNR precursor that results in magnetic QD structures embedded in semiconducting GNRs is reported. Inserting one such molecule into the GNR backbone and graphitizing it results in a QD region hosting one unpaired electron. QDs composed of two precursor molecules exhibit nonmagnetic, antiferromagnetic, or antiferromagnetic ground states, depending on the structural details that determine the coupling behavior of the spins originating from each molecule. The synthesis of these QDs and the emergence of localized states are demonstrated through high-resolution atomic force microscopy (HR-AFM), scanning tunneling microscopy (STM) imaging, and spectroscopy, and the relationship between QD atomic structure and magnetic properties is uncovered. GNR QDs provide a useful platform for controlling the spin-degree of freedom in carbon-based nanostructures.

1. Introduction

Graphene nanoribbons (GNRs) are promising candidates for future nanoelectronics applications owing to their exceptionally versatile electronic structure, transport properties, and spin coherence lengths/lifetimes.[1–7] An intriguing property of GNRs and other nanographenes is that the presence of localized electronic and magnetic states is sensitively dependent on atomistic parameters such as their edge structure and the presence of local sublattice imbalances.[8–19] The ability to regulate atomic-scale geometry by bottom-up synthesis strategies thus provides a useful tool for controlling the spin-degree of freedom inside GNRs, presenting new possibilities for realizing molecular spintronic, and quantum information devices.

While spin-based magnetism has been achieved in various molecular systems[9–11,20–28] including GNRs,[29–36] up to now no GNR precursor has been reported that can reliably deliver various spin configurations within a localized quantum dot (QD) region inside a GNR. This is a significant hindrance in the quest to fabricate GNRs with spatially controlled ferro- and antiferromagnetic regions from the bottom up.[37,38] Here we present a new GNR precursor that enables the synthesis of atomically precise magnetic QDs within semiconducting GNRs. We fabricated GNRs with embedded single-spin

P. H. Jacobse, Z. Wang, E. Berger, M. F. Crommie
Department of Physics
University of California, Berkeley
Berkeley, CA 94720, USA
E-mail: jacobse@berkeley.edu; crommie@berkeley.edu

M. Sarker, A. Sinitskii
Department of Chemistry
University of Nebraska
Lincoln, NE 68588, USA
E-mail: sinitskii@unl.edu

M. Sarker, A. Sinitskii
Nebraska Center for Materials and Nanoscience
University of Nebraska-Lincoln
Lincoln, NE 68588, USA

The ORCID identification number(s) for the author(s) of this article can be found under https://doi.org/10.1002/smll.202400473

DOI: 10.1002/smll.202400473

A. Saxena, N. R. Aluru
Walker Department of Mechanical Engineering
University of Texas
Austin, TX 78712, USA
E-mail: aluru@utexas.edu

A. Saxena, N. R. Aluru
Oden Institute for Computational Engineering and Sciences
University of Texas at Austin
Austin, TX 78712, USA

P. Zahl
Center for Functional Nanomaterials
Brookhaven National Laboratory
Upton, NY 11973, USA

Z. Wang, M. F. Crommie
Materials Sciences Division
Lawrence Berkeley National Laboratory
Berkeley, CA 94720, USA

Z. Wang, M. F. Crommie
Kavli Energy NanoSciences Institute at the University of California Berkeley and the Lawrence Berkeley National Laboratory
Berkeley, CA 94720, USA

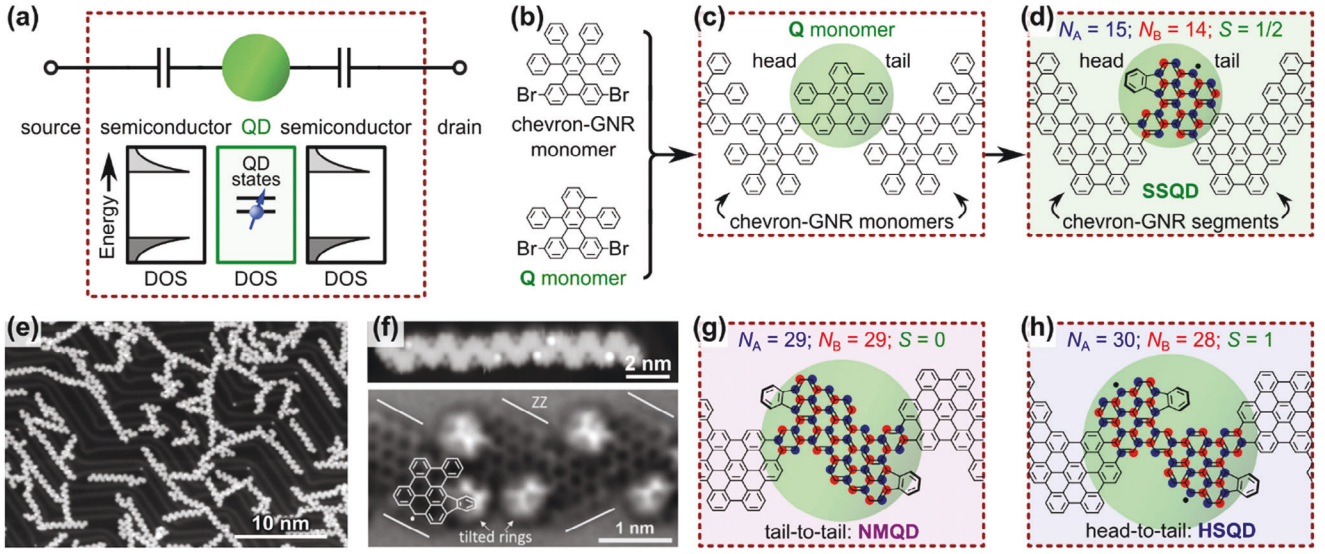

Figure 1. Design of GNR QDs. **a)** Schematic diagram of a hypothetical future device component utilizing GNR-based QD and semiconductor segments. **b)** Precursors (chevron-GNR and **Q**-monomer) used in this work to make GNR QDs. **c)** GNR single-spin quantum dot (SSQD) structure before cyclodehydrogenation showing one unit of **Q**-monomer sandwiched between chevron-GNR monomers. **d)** Final structure of a SSQD after cyclodehydrogenation. The blue and red disks label the two atomic sublattices. **e)** STM topographic overview image (V_s = −800 mV, I = 20 pA) of GNRs synthesized on Au(111) from the two precursors in **b**. **f)** The top panel shows an STM topographic image (V_s = −400 mV, I = 150 pA) of a single GNR. The bottom panel shows HR-AFM image acquired on a GNR showing 6 **Q**-monomers. The image shows the zigzag (ZZ) edges and the tilted benzene rings attached to the five-membered rings. One of the GNR segments is overlaid with its chemical structure. **g)** Structure of a nonmagnetic QD (NMQD) having S = 0 and comprising two **Q**-monomers coupled tail-to-tail. **h)** Structure of a high-spin QD (HSQD) having S = 1 and composed of two **Q**-monomers coupled head-to-tail. All STM/AFM data acquired at T = 4 K.

QDs (SSQDs), nonmagnetic QDs (NMQDs), antiferromagnetic QDs (AFQDs), and ferromagnetic QDs (FMQDs). We use scanning tunneling microscopy (STM), spectroscopy (STS), and high-resolution atomic force microscopy (HR-AFM) to characterize these structures and to analyze their (magnetic) characteristics. We show that the magnetic character of the QDs is determined by structural characteristics that affect local electron-electron interactions through a competition between exchange-coupling, hybridization, and Kondo-screening effects.

2. Results

2.1. Design and Synthesis of GNR QDs

Figure 1a shows a schematic illustration of a QD configuration where the QD is electronically separated from source and drain electrodes by semiconducting tunnel barriers. Implementing such a device component in a future nanoelectronics scheme could potentially be accomplished by sandwiching a GNR QD between two semiconducting GNR segments. We synthesized this type of structure by using a chevron-GNR as a wide-gap material for the tunnel barriers and a specially designed molecule 2,7-dibromo-9,14-diphenyl-10-methylbenzo[b]triphenylene (called the **Q**-monomer) as the "active core" of the QD (Figure 1b). A single methyl group in the **Q**-monomer breaks mirror symmetry and creates a sublattice imbalance upon cyclodehydrogenation as shown in the sketch of Figure 1d. Here the number of A sublattice sites N_A (highlighted in blue) outnumbers the number of B sublattice sites N_B (highlighted in red) by one, and so the ground state exhibits spin-1/2 by Lieb's theorem.[39,40] This QD structure is therefore referred to as a single-spin quantum dot (SSQD). The spin here emerges from the single unpaired p_z-electron associated with the unpaired carbon atom on the A sublattice. Because the mirror symmetry of the **Q**-monomer is broken we can identify a "head" side and a "tail" side of the molecule, with the head defined as the side with the five-membered ring and the tail defined as the side with the methyl group as shown in Figure 1c,d.

The **Q**-monomer was synthesized by condensation of 2-amino-3-methylbenzoic acid with 5,10-dibromo-1,3-diphenyl-2H-cyclopenta[l]phenanthren-2-one. Synthesis details are provided in the Supporting Information (Scheme S1 and Figure S1,S3 Supporting Information). The **Q**-monomer and chevron-GNR precursor molecule were co-deposited onto a Au(111) surface by sublimation from a Knudsen cell, after which Ullmann coupling was initiated by annealing the sample at T = 180 °C for t = 10 min. to polymerize the molecules (Figure S4, Supporting Information). The GNR synthesis was completed by a high-temperature cyclodehydrogenation reaction at T = 360 °C for t = 20 min. that converted the polymers into fully cyclized GNR heterostructures as shown in the top panel in Figure 1f. The sections hosting **Q**-monomers can be identified by their nonplanar character in STM topographs due to the benzene ring attached to the five-membered ring in the QD head protruding from the surface. This slight out-of-plane tilting was confirmed by high-resolution atomic force microscopy (HR-AFM). A HR-AFM image in Figure 1f shows a fragment of a GNR hosting a sequence of six **Q**-monomers. The image clearly shows the short zigzag-edge segments in the tail positions of the monomers as well as the protruding benzene rings, tilted relative to the plane of the

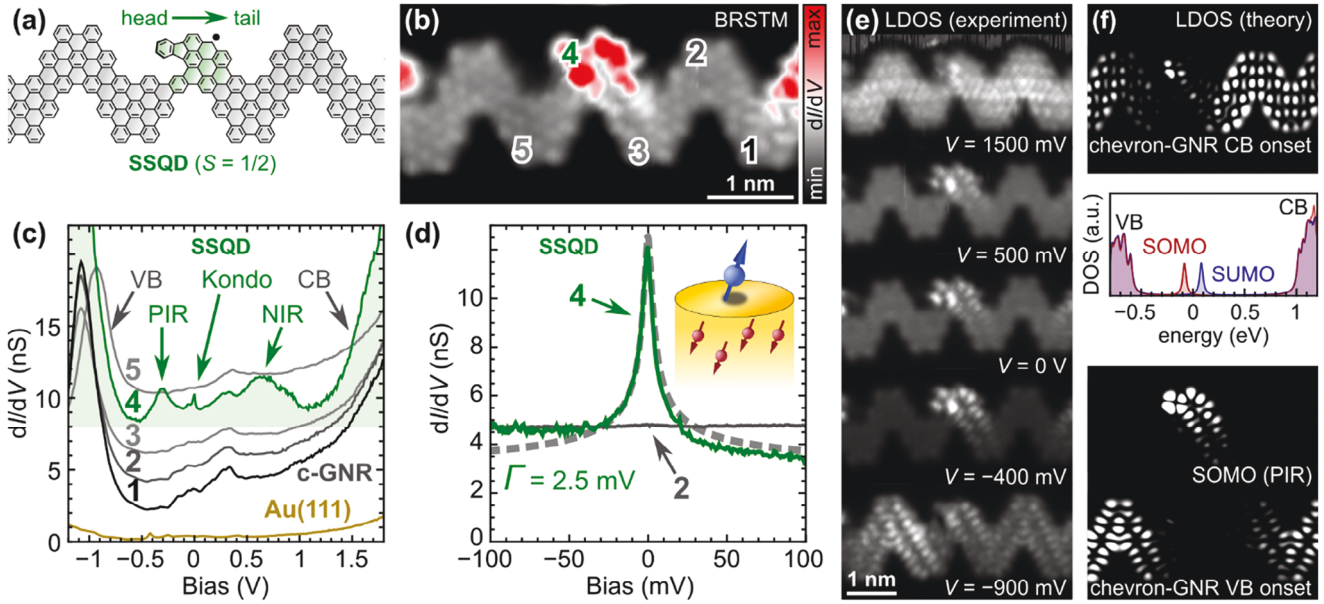

Figure 2. Single-spin quantum dots (SSQDs). **a)** Chemical structure of a SSQD composed of a single **Q**-monomer sandwiched by chevron-GNR. **b)** Constant-height BRSTM image of a SSQD whose core matches the model in **a** (V_s = 10 mV, V_{ac} = 20 mV). The numbers denote spectroscopy locations. **c)** dI/dV spectra acquired at numbered positions in **b** (V_{ac} = 1 mV). Sequential spectra are offset by increments of 2 nS for clarity. **d)** dI/dV spectra acquired at location 4 (green) and location 2 (gray) in **b**. **e)** Experimental constant height dI/dV maps acquired on the SSQD shown in **b** (V_{ac} = 20 mV). **f)** Simulated SSQD dI/dV maps corresponding to the CB edge (top), SOMO (middle), and VB edge (bottom). The inset shows the simulated spin-resolved density of states of the SSQD (red: spin up; blue: spin down).

ribbon likely because of H—H steric repulsions with the GNR backbone. HR-AFM imaging permits unambiguous identification of the GNR structure,[41–43] thus verifying that the cyclized form of the **Q**-monomer is the structure shown in Figure 1d.

Fusing two **Q**-monomers adjacent to one another leads to larger-scale QD structures that can differ depending on the relative orientation of the **Q**-monomers. For example, Figure 1g shows a "tail-to-tail" structure while Figure 1h shows a "head-to-tail" structure. A sublattice analysis of the tail-to-tail structure suggests that it exhibits $S = 0$ since the two sublattices balance exactly (Figure 1g). The head-to-tail structure on the other hand has a sublattice imbalance of $N_A - N_B = 2$, suggesting that it has net spin $S = 1$ according to Lieb's theorem (Figure 1h).[40] We refer to this as a high-spin QD (HSQD).

2.2. Single-Spin QDs

Figure 2a shows a chemical model of a SSQD where the QD section is highlighted in green and the chevron-GNR segments are shown in gray. A bond-resolved STM (BRSTM) image of a SSQD having this structure was obtained by recording the zero-bias differential conductance (dI/dV) at constant height using a carbon monoxide-passivated tip (Figure 2b).[44] Structural contrast in the chevron section can be seen with atomic resolution (gray areas), but the structure of the **Q**-monomer is obscured by electronic density of states that appears at low bias (red area).

dI/dV point spectroscopy of the SSQD is shown in Figure 2c (obtained at the numbered locations shown in Figure 2b). All the spectra show increased dI/dV for $V < -900$ mV and $V > 1500$ mV that we attribute to the onsets of the valence band (VB) and conduction band (CB), thus reflecting an energy gap of $E_g \approx 2.4$ eV (as seen previously for chevron-GNRs). The spectra obtained away from the QD (spectra 1, 2, 3, and 5) are relatively featureless in the energy gap region except for a small peak at $V = 300$ mV that is due to tip electronic structure. The spectrum obtained on the QD, however (spectrum 4) is very different and shows three new peaks at $V = -300$ mV, $V = 0$ mV, and $V = 700$ mV. The new filled state peak represents a positive ion resonance (PIR) localized on the QD whereas the empty state peak represents a negative ion resonance (NIR).

To identify the peak at $V = 0$ mV we show a higher resolution spectrum obtained on the QD at point 4 in Figure 2d. This peak is much narrower than the PIR or NIR and has a half-width at half maximum (HWHM) of only $\Delta V = (6.4 \pm 0.8)$ mV when fitted with a Frota function.[45] We identify this as a Kondo resonance arising from the screening of the SSQD spin by the Au(111) surface.[30,46] The presence of the Kondo resonance explains why the bonding structure of the QD is washed out in the low-bias BRSTM image of Figure 2b (red area).

The SSQD electronic structure was further characterized using dI/dV mapping that resolves the wavefunction pattern of electronic states through the local density of states (LDOS) (Figure 2f).[47] dI/dV maps acquired at the conduction (1500 mV) and valence (−900 mV) band edges show highly delocalized wavefunction density across the entire GNR, as expected for band states. dI/dV maps taken at energies near the PIR (−400 mV), the Kondo resonance (0 mV), and the NIR (1500 mV), however, show very different behavior. Here the dI/dV maps have low density except in the QD region, which shows high intensity. The dI/dV intensity seen in the QD area has a distinctive nodal pattern that is identical for each of the maps taken at the PIR, Kondo

resonance, and NIR energies, suggesting that these three experimental features all arise from the same quantum state.

The origin of these spectroscopic features can be determined by comparing our experimental dI/dV maps to the results of *ab-initio* density functional theory (DFT) calculations, as shown in Figure 2f. The second panel in Figure 2f shows the total density of states (DOS) calculated for a SSQD GNR having the same structure as in Figure 2a (additional details can be found in Figure S5, Supporting Information). VB and CB edges are seen at E = −600 meV and E = 1000 meV, respectively, leading to a predicted bandgap of E_g = 1.6 eV. The theoretical LDOS at the energies of the CB and VB edge is shown to be highly delocalized across the GNR and to have low intensity in the QD region, similar to the experimental band edge dI/dV maps of Figure 2e. The predicted ground state of the SSQD is an open-shell doublet, which leads to a singly occupied molecular orbital (SOMO) at −100 meV and a singly unoccupied molecular orbital (SUMO) at 100 meV. The spatially resolved LDOS for the SOMO is shown in the third panel of Figure 2f and is indistinguishable from the SUMO (Figure S5, Supporting Information). The theoretical SOMO/SUMO closely match the experimental state density of Figure 2e. These states have identical wavefunction patterns since they both arise from the same QD orbital and differ only by electron occupancy.[32,48] Kondo features typically match the spatial pattern of the SOMO and SUMO, as is the case here.[49] The precise energies of the theoretical states differ from the experimental states, but the trends are the same and this is consistent with previous DFT results that are known to underestimate energy gaps.[50]

2.3. S = 0 Quantum Dots

When two **Q**-monomers are included in a QD then the total QD spin can be either smaller or larger than the S = ½ SSQD described above, depending on structural details. Here we describe two different QD structures that both yield QDs with a net spin of S = 0. The first involves tail-to-tail coupling of **Q**-monomers and can be seen in the sketch of **Figure 3a**. This structure exhibits a closed-shell electronic ground state and is referred to as a nonmagnetic QD (NMQD). Figure 3c shows an experimental BRSTM image of an NMQD structure bracketed by chevron-GNR segments (the **Q**-monomer locations are labeled "2" and "3" in the image).

Figure 2e shows point spectroscopy obtained for the NMQD at the positions marked in Figure 3c.The dI/dV signal is seen to rise steeply at energies corresponding to the CB and VB edges across the entire GNR. At the NMQD site, however, the dI/dV shows two pronounced peak features centered roughly at V = −500 mV and V = 500 mV. The spatial dependence of these features was obtained from dI/dV maps taken at V = ±350 mV, the onset voltages of the two peak features. As seen in Figure 3g, the NMQD structure lights up at these voltages, indicating that the peaks at V = ±500 mV are localized states associated with the NMQD.

We are able to understand the origin of the experimental STS features by comparing our data to the results of *ab-initio* DFT calculations. Figure 3h shows the calculated DOS for the same structure shown in Figure 3a. Broad VB and CB features are seen at the energies expected for a chevron-GNR, but two new peaks are observed at E = ±250 meV. The DFT calculation returns a nonmagnetic ground state for the NMQD. The DOS peak at E = −250 meV contains two electrons of opposite spin and is the highest occupied molecular orbital (HOMO) whereas the peak at E = 250 meV is the lowest unoccupied molecular orbital (LUMO). The theoretical wavefunction patterns of the HOMO and LUMO can be seen in the rightmost panels of Figure 3g. The nodal patterns of these two states are different since they are completely different orbitals (unlike the SOMO and SUMO seen for the magnetic SSQD). Comparison of our experimental data to the DFT results implies that the experimental peaks seen at V = ±500 mV in Figure 3e are the HOMO and LUMO of the NMQD. Further evidence comes from the fact that the experimental nodal pattern seen at V = −350 mV looks very similar to the theoretical HOMO, whereas the dI/dV map at V = 350 mV resembles the theoretical LUMO. An intuitive explanation of the NMQD electronic structure is that the zero-modes arising from the sublattice imbalance of the two constituent **Q**-monomers are strongly hybridized (this coupling is represented by the t in Figure 3a). The HOMO can therefore be thought of as the bonding orbital between the two zero-modes whereas the LUMO is the antibonding orbital.[18]

A second S = 0 QD structure is shown in Figure 3b and consists of two **Q**-monomers bridged by a single chevron monomer. This structure exhibits an open-shell electronic structure where each **Q**-monomer yields a single electron spin and the two spins are coupled antiferromagnetically. This structure is thus named an antiferromagnetic QD (AFQD). A BRSTM image of an AFQD having the same structure as in Figure 3b is shown in Figure 3d (positions 2 and 4 mark the locations of the cyclized **Q**-monomers). dI/dV point spectroscopy of the AFQD shows the expected band edge features of a chevron-GNR, but also shows two new peaks centered at V = −400 mV and V = +700 mV, that are localized to the **Q**-monomer sites (Figure 3f). A small zero-bias anomaly (ZBA) can also be seen in the dI/dV spectra at the sites of the **Q**-monomers. High-resolution spectroscopy of the ZBA from position 4 is shown in Figure 3i and exhibits a clear pseudogap structure with a full width at half maximum (FWHM) of ≈20 mV.

This behavior is consistent with the AFQD having a magnetic ground state where each cyclized **Q**-monomer contains a single net spin and the two spins are antiferromagnetically coupled.[10,11,20–26,30,36] The main evidence for this is the V = 0 pseudogap feature seen in the point spectroscopy. This feature can be explained by inelastic tunneling that occurs when tunneling electrons are provided enough energy to excite the singlet S = 0 ground state of the AFQD to a higher-energy triplet state (S = 1). This process can be simulated using a straightforward model by Ternes that leads to a good fit to the spectrum for a magnetic coupling constant of J = 9.2 meV (Figure 3h, gray dashed line).[51] Further evidence for a magnetic ground state is that the wavefunctions for the resonances at V = −400 mV and V = 600 mV look very similar (Figure S7, Supporting Information). This suggests that these peaks arise from positive (SOMOs) and negative (SUMOs) ion resonances derived from the *same* orbital rather than from a *different* HOMO and LUMO as expected for a closed-shell nonmagnetic ground state (Figure S6f, Supporting Information). We note that our DFT simulation of the AFQD actually yielded a nonmagnetic ground state in contrast to our conclusions here (Figure S6e,f, Supporting Information). A possible

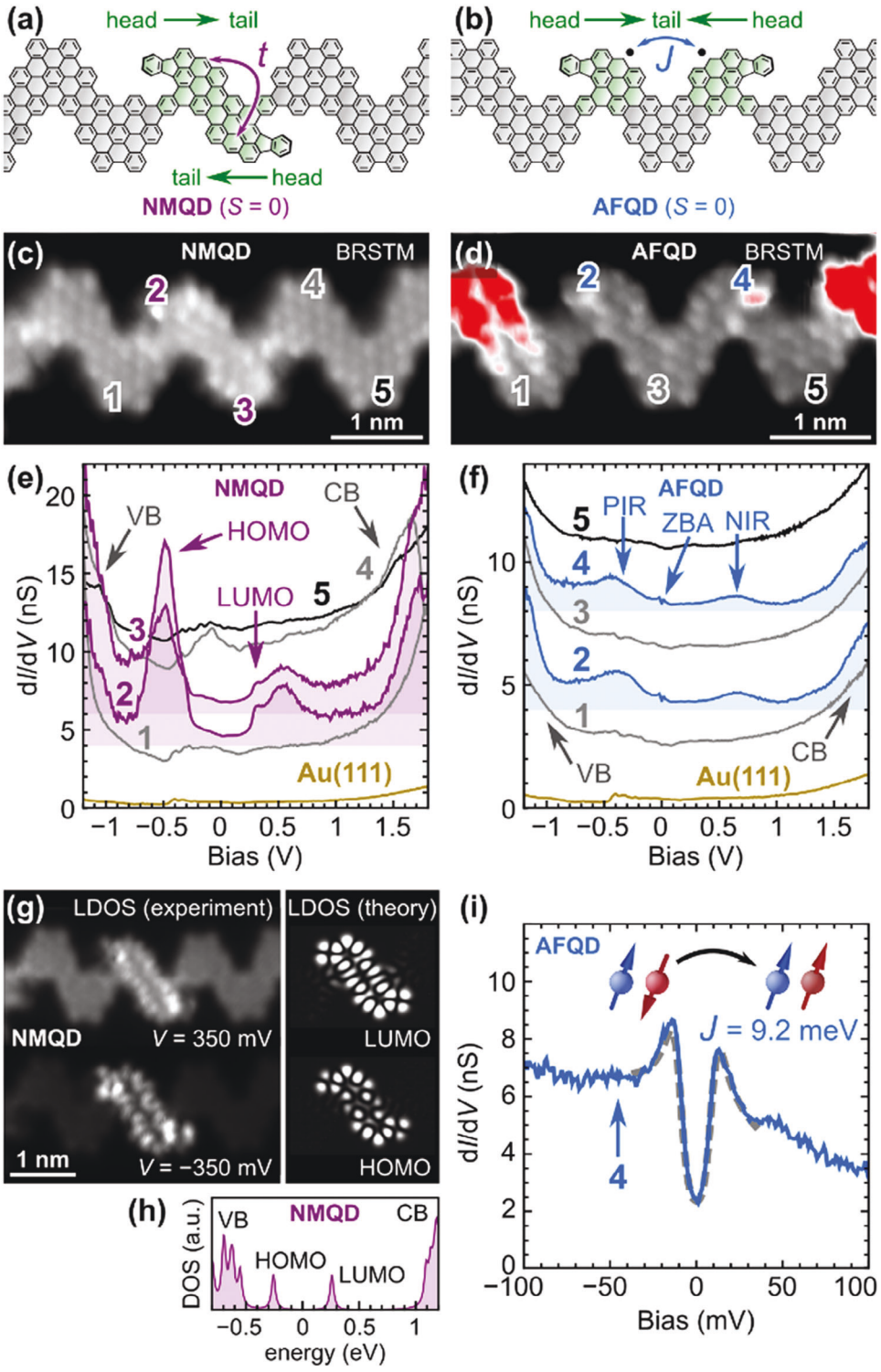

Figure 3. Low-spin quantum dots. **a)** Model of the nonmagnetic QD (NMQD) having two **Q**-monomers directly attached tail-to-tail. **b)** Model of the antiferromagnetic QD (AFQD) having two **Q**-monomers separated by one chevron-GNR monomer. **c)** BRSTM scan of the NMQD (V_s = 10 mV, V_{ac} = 20 mV). The numbers denote spectroscopy locations **d)** BRSTM scan of the large LSQD (V_s = 0 mV, V_{ac} = 20 mV). The numbers denote spectroscopy locations. **e)** d*I*/d*V* spectra acquired on the NMQD. Sequential spectra are offset by increments of 2 nS for clarity. **f)** d*I*/d*V* spectra acquired on the AFQD at the numbered locations in **d**. Sequential spectra are offset by increments of 2 nS for clarity. **g)** Experimental (left panel, V_{ac} = 20 mV) and simulated (right panel) d*I*/d*V* maps of the NMQD. **h)** Simulated density of states of the NMQD using DFT. **i)** d*I*/d*V* spectrum acquired at location 4 of the AFQD (blue, V_{ac} = 1 mV) and fit using the Ternes model for two antiferromagnetically coupled spins (dashed).

reason for this is that magnetism is somehow stabilized by the Au(111) surface (that is not included in our simulation).

2.4. High-Spin Quantum Dots

We have also observed magnetic QD structures where two **Q**-monomers are bonded head-to-tail, thus leading to ferromagnetic coupling (i.e., $S = 1$) between the electrons residing on each cyclized **Q**-monomer (here the sublattice imbalance resides on the same sublattice for each **Q**-monomer). We see two different configurations of high-spin QDs (HSQDs) as shown in **Figure 4**a,b. The most common is termed the "regular" HSQD (Figure 4a), whereas the second is the "defective" HSQD (D-HSQD) (Figure 4b). The D-HSQD is identical to the HSQD except that it is missing a single benzene ring at the location of the black arrow in Figure 4b. This causes the linkage between the QD and right chevron segment to be greatly reduced for the D-HSQD compared to the HSQD.[52] Figure 4c,d show experimental BRSTM images of a HSQD GNR and a D-HSQD GNR having the same structures as sketched in Figure 4a,b. STM spectroscopy of both the HSQD (Figure 4e) and the D-HSQD (Figure 4f) show band edge features due to the VB and CB edges, as well as filled and empty state resonances at $V = \pm 500$ mV that are localized to the sites of the cyclized **Q**-monomers. Both also exhibit narrow Kondo-like resonances at $V = 0$ mV. A difference between the two types of QDs, however, is the lineshape of the $V = 0$ resonance. The HSQD has what appears to be a typical narrow Kondo resonance (Figure 4g) whereas the D-HSQD has a narrow central peak that is flanked by a shoulder on each side of $V = 0$ (Figure 4h) (Similar features have been reported for ferromagnetically coupled spins in chiral GNRs[36] and rhombene chains.[21])

The behavior of HSQDs and D-HSQDs can be understood by considering how the spins originating from the **Q**-monomers couple to their environment. DFT simulations of the two structures both yield magnetic ground states with $S_{\text{total}} = 1$ and SOMO/SUMO that look similar to the experimental $\mathrm{d}I/\mathrm{d}V$ maps (Figures S7,S8 Supporting Information). This is consistent with the simple sublattice analysis of Figure 1h. The Kondo resonance seen for the HSQD likely arises from the spin in each **Q**-monomer of the QD being independently screened via a substrate-induced Kondo effect. This is expected if the J-coupling between the two spins is less than the Kondo binding energy for a single spin, $k_B T_K$.[33,35] Each **Q**-monomer then produces a single Kondo peak that can be fitted by a Frota function with a HWHM of 6.9 meV (resulting in $T_K \approx 85$ K).[45] The D-HSQD data however is consistent with the J-coupling between the two spins being higher due to increased quantum confinement of the QD state on the right-hand side. This causes the J-coupling to surpass the single-spin T_K, and so the two spins couple into a net $S = 1$ spin for the *entire* QD that is then Kondo-screened by the substrate.[21,36] Kondo screening in this cases contributes to the central peak. The shoulders occur when the voltage of a tunneling electron is large enough to induce a triplet-to-singlet spin excitation, thus leading to an inelastic tunneling enhancement in the current. These features arise naturally in the perturbative Kondo model by Ternes and fit the D-HSQD lineshape quite well for a ferromagnetic coupling constant between the two spins of $J = -6.4$ meV (dashed line in Figure 4h).[51] Such behavior is consistent with what is observed by de Oteyza et al. for ferromagnetically coupled pairs of spins inside GNRs.[36]

3. Conclusion

While Lieb's theorem can be used to predict the total spin of GNR QDs, it falls short of explaining all of the magnetic behavior observed in our experimental data, which also includes coupling to the substrate. An intuitive rationalization of these variations is to consider the overlap between zero-mode wavefunctions that depends on how **Q**-monomers are separated, their orientation, and the presence of defects.[20,21,53–55] **Figure 5**a shows how the relative orientation of **Q**-monomers affects the number of bonds connected to them, which in turn modulates the degree of delocalization of the zero-mode wavefunctions associated with each cyclized **Q**-monomer. Because the number of bonds attached to the tail side of a **Q**-monomer (3) is larger than the maximum number to its head side (2), the zero-mode wavefunction spreads out asymmetrically as shown in Figure 5b. Here the exponential decay of the zero-mode wavefunction spreads further into the tail side, which has more connecting bonds. When a defect is present (i.e., a missing benzene ring) on the tail-side chevron segment then the number of bonds on that side is reduced and the wavefunction becomes more "compressed" (Figure 5c).

In the case of $S = 0$ QDs (Figure 5d) the magnetic character is determined by a competition between the hybridization interaction t between **Q**-monomers and the Coulomb repulsion U. When **Q**-monomers are directly connected tail-to-tail as in the NMQD, the high connectivity creates a large wavefunction overlap that translates into a large hybridization interaction t so that $t > U$.[6,10,53–55] This causes the NMQD zero-modes to gap out into bonding and antibonding combinations that become the HOMO and LUMO. Separating the **Q**-monomers by a single chevron-GNR unit as in the AFQD reduces the zero-mode wavefunction overlap so that the hybridization interaction t becomes smaller than the Coulomb repulsion U. This results in an open-shell magnetic ground state that adopts an antiferromagnetic configuration because the **Q**-monomers sit on opposite sublattices.[11,40] The **Q**-monomers in this case are not Kondo-screened since the magnetic coupling ($J = 9.2$ meV) is ostensibly larger than the competing Kondo binding energy $k_B T_K$.

For HSQDs the dominant competition is between the inter-spin J-coupling and the Kondo binding energy $k_B T_K$ to the metallic substrate.[35,56,57] In the case of the regular HSQD the Kondo screening prevails and the two spins are individually screened (Figure 5e). For the defective HSQD, however, the zero-mode wavefunction on the tail-end side of the HSQD is compressed due to a reduction of connective bonds. This likely causes an increase in the overlap between the two zero-mode wave functions and a corresponding increase in J. As a result, the exchange coupling dominates over the Kondo screening and the spins form a triplet ground state (Figure 5f).

To conclude, we have synthesized magnetic GNR QDs by combining a new zero-mode-generating precursor (termed **Q**-monomer) with semiconducting chevron-GNR precursors. Different relative orientations and positions of **Q**-monomers produce low-spin and high-spin QDs that arise due to the different magnetic coupling environments experienced by the spins on each **Q**-monomer. The behavior of the resulting magnetic

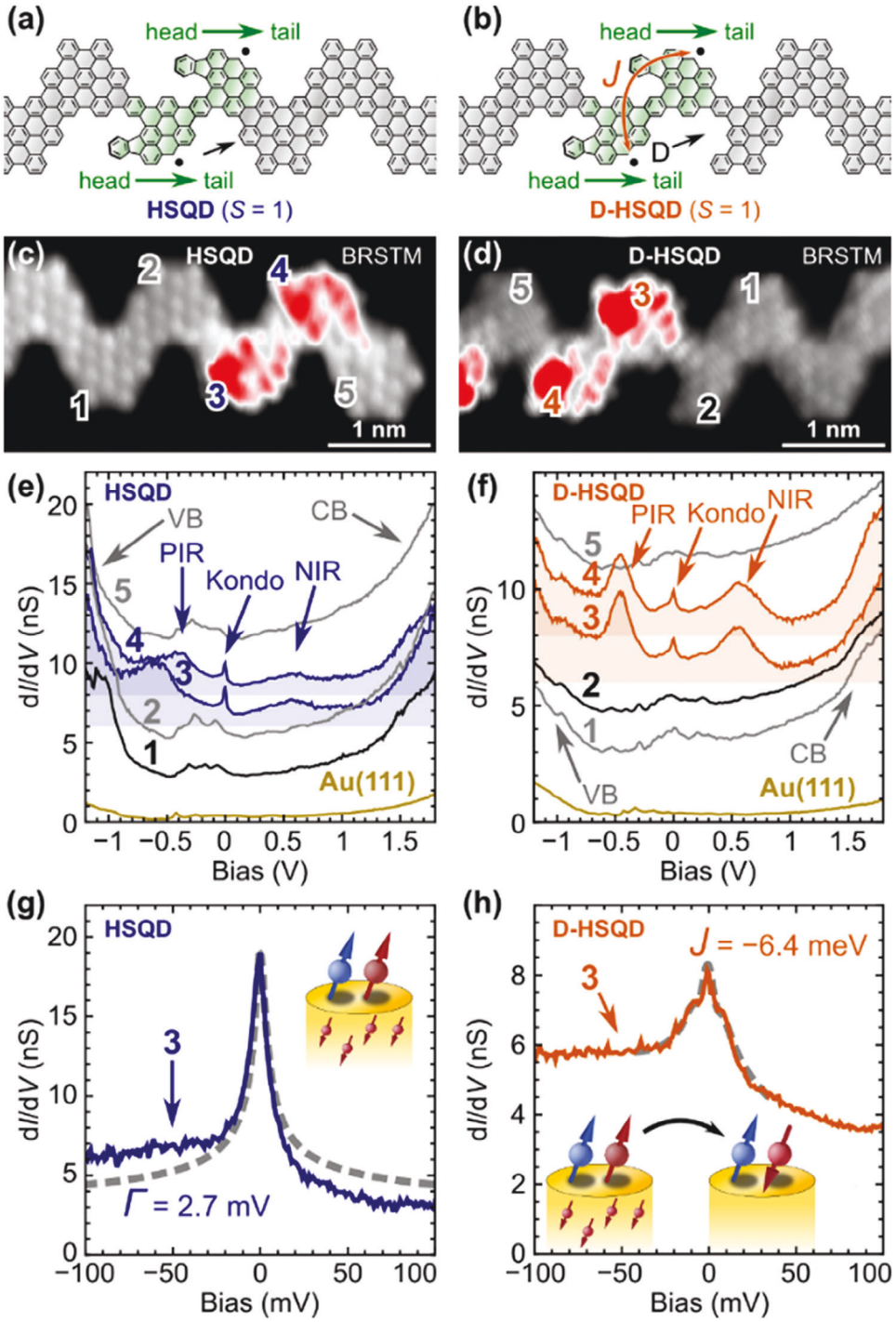

Figure 4. High-spin quantum dots (HSQDs). **a)** Model of a regular HSQD with two **Q**-monomers directly attached head-to-tail. **b)** Model of a defective HSQD (D-HSQD) having one benzene ring missing (denoted by D) in the chevron-GNR monomer next to the **Q**-monomer. **c)** BRSTM scan of the HSQD ($V_s = 0$ mV, $V_{ac} = 20$ mV). The numbers denote spectroscopy locations. **d)** BRSTM scan of the D-HSQD ($V_s = 0$ mV, $V_{ac} = 20$ mV). The numbers denote spectroscopy locations. **e)** d*I*/d*V* spectra acquired on the HSQD at the marked locations shown in **c** ($V_{ac} = 1$ mV). Sequential spectra are offset by increments of 2 nS for clarity. **f)** d*I*/d*V* spectra acquired on the D-HSQD at the locations shown in **d**. Sequential spectra are offset by increments of 2 nS for clarity. **g)** d*I*/d*V* spectrum acquired at location 3 of the HSQD shown in **c** ($V_{ac} = 1$ mV, blue line) and fit using the Frota lineshape (dashed). **h)** d*I*/d*V* spectrum acquired at location 3 of the D-HSQD shown in **d** ($V_{ac} = 1$ mV, orange line) and fit using Ternes' theory for two ferromagnetically coupled spins (dashed).

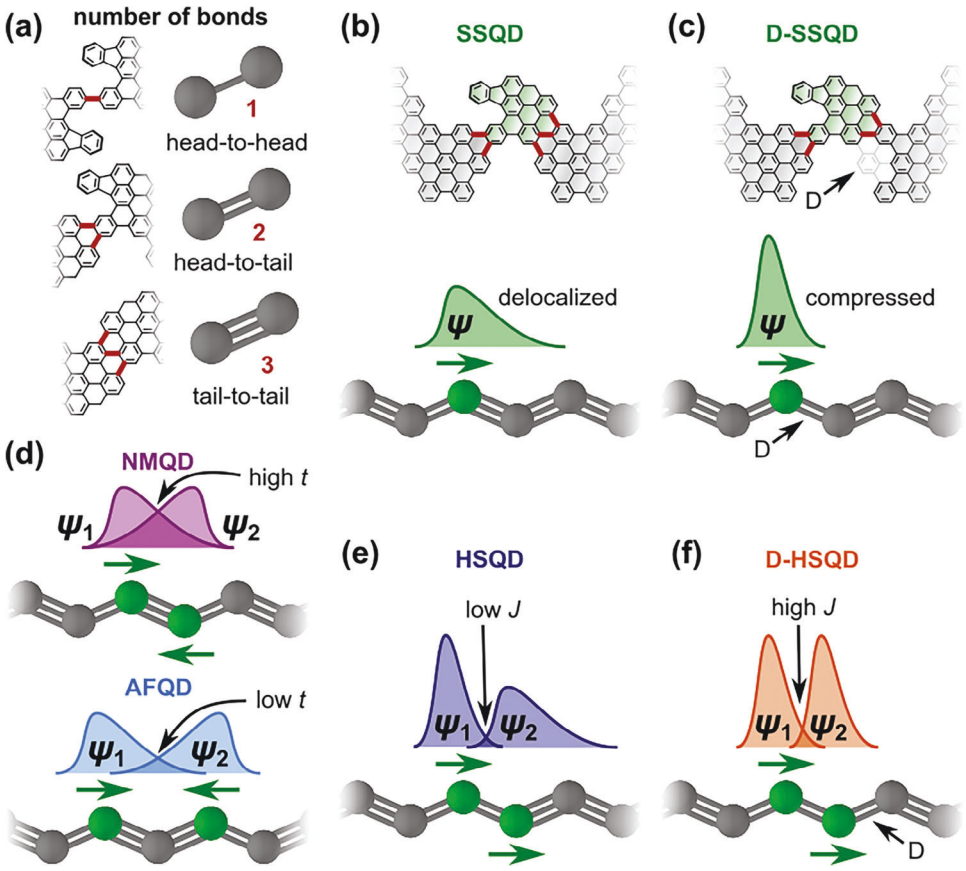

Figure 5. Schematic rationalization for magnetic dependence on wavefunction overlap. **a)** The number of carbon-carbon bonds between **Q**-monomers connected head-to-head, head-to-tail, and tail-to-tail. **b)** Effective ball-and-stick model of **Q**-monomer connectivity and schematic wavefunction (green curve) for the SSQD. **c)** **Q**-monomer connectivity and schematic wavefunction (green curve) for a defective SSQD. **d)** **Q**-monomer connectivity and schematic wavefunctions (purple and blue curves) for low-spin QDs. **e)** **Q**-monomer connectivity and schematic wavefunction (blue curve) for the HSQD. **f)** **Q**-monomer connectivity and schematic wavefunction (orange curve) for the D-HSQD. Here decreased connectivity causes increased localization of the zero-mode wave function on the right **Q**-monomer, thus increasing zero-mode wavefunction overlap and ferromagnetic coupling.

GNR QDs can be rationalized by combining Lieb's theorem with the competition between hybridization, Coulomb interaction, exchange coupling, and Kondo screening. Although the synthesis was performed on an Au(111) surface, the compatibility of the **Q**-monomer with the chevron-GNR precursor suggests it may also be amenable to solution-based GNR synthesis techniques, which additionally paves the way to precise sequence control.[58] The ability to create bottom-up fabricated GNR QDs with tunable magnetic ground states brings new possibilities for engineering future molecule-based spintronic devices.

4. Experimental Section

Precursor Synthesis: All the starting materials and reagents used were purchased from commercial sources and used without further purification unless otherwise noted. The dry solvent 1,2-dichloro-ethane (DCE) was freshly distilled, employing a standard method before use.[59] First 5,10-dibromo-1,3-diphenyl-2H-cyclopenta[l]phenanthren-2-one **1**) was synthesized according to a reported procedure.[59] Then reaction of compound **1** with 2-amino-3-methylbenzoic acid yielded 2,7-dibromo-9,14-diphenyl-10-methylbenzo[b]triphenylene (**Q**-monomer) as a light-yellow product. ^{1}H-NMR (400 MHz, $CDCl_3$, δ): 8.00 (dd, 2H, and Ar—H), 7.74 (d, 1H, and Ar—H), 7.56-7.47 (m, 11 H, and Ar—H), 7.41-7.34 (m, 3H, and Ar—H), 7.30 (d, 1H, and Ar—H), 7.23 (d, 1H, and Ar—H), 1.90 (s, 3H, and methyl-H) ppm. ^{13}C-NMR (100 MHz, $CDCl_3$, and δ): 142.68, 140.71, 136.01, 135.91, 135.86, 133.39, 133.21, 133.03, 132.92, 132.87, 132.55, 130.55, 130.22, 129.80, 129.78, 129.58, 129.16, 128.31, 128.24, 126.97126.87, 125.92, 125.06, 124.77, 124.54, 120.49, 120.02, and 24.43 (methyl-C), ppm. HR-MS (MALDI-TOF, DCTB Matrix), m/z: 602.011468 (calculated 602.01). Chemical shifts are stated in parts per million (ppm, δ), downfield from tetramethyl silane (TMS, $\delta = 0.00$ ppm) and were referenced to residual solvent ($CDCl_3$, $\delta = 7.26$ ppm (^{1}H) and 77.00 ppm (^{13}C). Synthesis details are provided in the Supporting Information.

Sample Preparation: QD GNRs were prepared by on-surface synthesis under UHV conditions on Au(111)/mica films for STM and STS measurements and on an Au(111) single crystal for HR-AFM measurements. Atomically clean Au(111) surfaces were prepared through iterative cycles of Ar^+ bombardment at 1 kV and 2 to 4 μA current and annealing under UHV conditions at $T = 450$ to 550 °C. Sub-monolayer coverages of chevron-GNR precursor and **Q**-monomer were obtained by sublimation from homebuilt Knudsen cell evaporators at crucible temperatures of 160–200 °C. Radical step-growth polymerization was achieved by heating the molecule-decorated surface to a temperature of 180 °C. Further heating to $T = 360$ °C for $t = 20$ min was performed to induce cyclodehydrogenation.

Scanning Probe Measurements: All STM experiments were performed using a commercial CreaTec LT-STM operating at $T = 4$ K at a base pressure below $7{\cdot}10^{-10}$ mbar using tungsten STM tips. All HR-AFM experiments

were performed using a CreaTec STM with home-made modifications to provide HR-AFM capabilities, operating at $T = 4$ K using qPlus sensors. The base pressure for this system was below $7{\cdot}10^{-11}$ mbar. The HR-AFM was operated using Gxsm3 software and custom MK3-A810/HighSpeed RedPAC-PLL hardware. STS and d*I*/d*V* mapping were all performed under open feedback loop conditions (constant height) using a lock-in amplifier supplying a modulation voltage of $V_{ac} = 500$ µV for point spectroscopy and 10 mV $\leq V_{ac} \leq$20 mV for mapping at a frequency of 533 Hz. Tip passivation was achieved by controlled attachment of individual carbon monoxide molecules deposited onto the surface by gas dosing.[60] Image processing of the STM scans was performed using WSxM software.[61] Fitting of Kondo line shapes was performed using the Frota equation $T\ (E) = T_0\ - A\ \mathrm{Re}[\sqrt{\frac{i\Gamma_F}{E+i\Gamma_F}}]$.[35,45] The extracted Frota parameters were converted to HWHM values using $\Gamma_{\mathrm{HWHM}} \approx 2.54\Gamma_F$. Finally, the Kondo temperature was estimated using $k_B T_K \approx \Gamma_{\mathrm{HWHM}}$.

Calculations: Density functional theory (DFT) calculations were performed for the QD GNRs using VASP.[62] Projector augmented wave (PAW) pseudopotentials[63] with a 450 eV energy cutoff were used with the local density approximation (LDA) exchange-correlation functional.[64,65] The structural relaxation and density of states calculations were performed using a gamma-centered 4 × 1 × 1 and 8 × 1 × 1 k-point grid, respectively. 15 Å of vacuum was applied in the non-periodic directions. Force convergence criteria of 0.01 eV Å^{-1} and energy convergence criteria of 1×10^{-6} eV were used. The local density of states (LDOS) calculations were performed using Quantum Espresso.[66] Norm-conserving Vanderbilt pseudopotentials[67] were used to construct the wavefunctions with a plane-wave kinetic energy cutoff of 60 Ry. The wavefunction density was calculated at a distance of 2 Å above the GNR plane. Visualization of the LDOS was performed with XCrysDen.[68]

Supporting Information

Supporting Information is available from the Wiley Online Library or from the author.

Acknowledgements

P.H.J., M.S., and A.S. contributed equally to this work. This work was supported by the Office of Naval Research award N00014-19-1-2596 (STM imaging, molecular synthesis) and by the US Department of Energy (DOE), Office of Science, Basic Energy Sciences (BES), the Materials Sciences and Engineering Division under contract DE-AC02-05-CH11231 (Nanomachine program KC1203) (local spectroscopy). The research was also supported by the National Science Foundation under Grant No. CHE-2204252 (molecular image analysis). This research used the LT-STM/HR-AFM facility of the Center for Functional Nanomaterials (CFN), which is a U.S. Department of Energy Office of Science user facility, at the Brookhaven National Laboratory under contract No. DE-SC0012704. The authors acknowledge the use of the parallel computing resource Lonestar6 provided by the Texas Advanced Computing Center (TACC) at The University of Texas at Austin.

Conflict of Interest

The authors declare no conflict of interest.

Data Availability Statement

The data that support the findings of this study are available from the corresponding author upon reasonable request.

Keywords

magnetism, Quantum dots, spin, graphene nanoribbons

Received: January 20, 2024
Published online: February 27, 2024

[1] Q. Sun, O. Gröning, J. Overbeck, O. Braun, M. L. Perrin, G. Borin Barin, M. El Abbassi, K. Eimre, E. Ditler, C. Daniels, V. Meunier, C. A. Pignedoli, M. Calame, R. Fasel, P. Ruffieux, *Adv. Mater.* **2020**, *32*, 1906054.
[2] L. Talirz, P. Ruffieux, R. Fasel, *Adv. Mater.* **2016**, *28*, 6222.
[3] J. Baringhaus, M. Ruan, F. Edler, A. Tejeda, M. Sicot, A. Taleb-Ibrahimi, A.-P. Li, Z. Jiang, E. H. Conrad, C. Berger, C. Tegenkamp, W. A. de Heer, *Nature* **2014**, *506*, 349.
[4] S. Zamani, R. Farghadan, *Phys. Rev. Appl.* **2018**, *10*, 34059.
[5] Y. Gu, Z. Qiu, K. Müllen, *J. Am. Chem. Soc.* **2022**, *144*, 11499.
[6] M. J. J. Mangnus, F. R. Fischer, M. F. Crommie, I. Swart, P. H. Jacobse, *Phys. Rev. B* **2022**, *105*, 115424.
[7] A. K. Geim, K. S. Novoselov, *Nat. Mater.* **2007**, *6*, 183.
[8] M. Fujita, K. Wakabayashi, K. Nakada, K. Kusakabe, *J. Phys. Soc. Jpn.* **1996**, *65*, 1920.
[9] O. V. Yazyev, *Rep. Prog. Phys.* **2010**, *73*, 056501.
[10] D. G. de Oteyza, T. Frederiksen, *J. Phys. Condens. Matter* **2022**, *34*, 443001.
[11] S. Song, J. Su, M. Telychko, J. Li, G. Li, Y. Li, C. Su, J. Wu, J. Lu, *Chem. Soc. Rev.* **2021**, *50*, 3238.
[12] T. Cao, F. Zhao, S. G. Louie, *Phys. Rev. Lett.* **2017**, *119*, 076401.
[13] O. Gröning, S. Wang, X. Yao, C. A. Pignedoli, G. Borin Barin, C. Daniels, A. Cupo, V. Meunier, X. Feng, A. Narita, K. Müllen, P. Ruffieux, R. Fasel, *Nature* **2018**, *560*, 209.
[14] D. J. Rizzo, G. Veber, T. Cao, C. Bronner, T. Chen, F. Zhao, H. Rodriguez, S. G. Louie, M. F. Crommie, F. R. Fischer, *Nature* **2018**, *560*, 204.
[15] L. Yan, P. Liljeroth, *Adv. Phys. X* **2019**, *4*, 1651672.
[16] Y. L. Lee, F. Zhao, T. Cao, J. Ihm, S. G. Louie, *Nano Lett.* **2018**, *18*, 7247.
[17] Q. Sun, Y. Yan, X. Yao, K. Müllen, A. Narita, R. Fasel, P. Ruffieux, *J. Phys. Chem. Lett.* **2021**, *12*, 8679.
[18] D. J. Rizzo, J. Jiang, D. Joshi, G. C. Veber, C. Bronner, R. A. Durr, P. H. Jacobse, T. Cao, A. M. Kalayjian, H. Rodriguez, P. Butler, T. Chen, S. G. Louie, F. R. Fischer, M. F. Crommie, *ACS Nano* **2021**, *15*, 20633.
[19] D. J. Rizzo, G. Veber, J. Jiang, R. McCurdy, T. Cao, C. Bronner, T. Chen, S. G. Louie, F. R. Fischer, M. F. Crommie, *Science* **2020**, *369*, 1597.
[20] S. Mishra, D. Beyer, K. Eimre, R. Ortiz, J. Fernández-Rossier, R. Berger, O. Gröning, C. A. Pignedoli, R. Fasel, X. Feng, P. Ruffieux, *Angew. Chem., Int. Ed.* **2020**, *59*, 12041.
[21] Y. Zheng, C. Li, C. Xu, D. Beyer, X. Yue, Y. Zhao, G. Wang, D. Guan, Y. Li, H. Zheng, C. Liu, J. Liu, X. Wang, W. Luo, X. Feng, S. Wang, J. Jia, *Nat. Commun.* **2020**, *11*, 6076.
[22] J. Li, S. Sanz, J. Castro-Esteban, M. Vilas-Varela, N. Friedrich, T. Frederiksen, D. Peña, J. I. Pascual, *Phys. Rev. Lett.* **2020**, *124*, 177201.
[23] S. Mishra, D. Beyer, K. Eimre, S. Kezilebieke, R. Berger, O. Gröning, C. A. Pignedoli, K. Müllen, P. Liljeroth, P. Ruffieux, X. Feng, R. Fasel, *Nat. Nanotechnol.* **2020**, *15*, 22.
[24] S. Mishra, X. Yao, Q. Chen, K. Eimre, O. Gröning, R. Ortiz, M. Di Giovannantonio, J. C. Sancho-García, J. Fernández-Rossier, C. A. Pignedoli, K. Müllen, P. Ruffieux, A. Narita, R. Fasel, *Nat. Chem.* **2021**, *13*, 581.
[25] S. Mishra, G. Catarina, F. Wu, R. Ortiz, D. Jacob, K. Eimre, J. Ma, C. A. Pignedoli, X. Feng, P. Ruffieux, J. Fernández-Rossier, R. Fasel, *Nature* **2021**, *598*, 287.
[26] J. Hieulle, S. Castro, N. Friedrich, A. Vegliante, F. R. Lara, S. Sanz, D. Rey, M. Corso, T. Frederiksen, J. I. Pascual, D. Peña, *Angew. Chem., Int. Ed.* **2021**, *60*, 25224.

[27] S. Cheng, Z. Xue, C. Li, Y. Liu, L. Xiang, Y. Ke, K. Yan, S. Wang, P. Yu, *Nat. Commun.* **2022**, *13*, 1705.
[28] Q. Sun, L. M. Mateo, R. Robles, P. Ruffieux, G. Bottari, T. Torres, R. Fasel, N. Lorente, *Adv. Sci.* **2022**, *9*, 2105906.
[29] M. Slota, A. Keerthi, W. K. Myers, E. Tretyakov, M. Baumgarten, A. Ardavan, H. Sadeghi, C. J. Lambert, A. Narita, K. Müllen, L. Bogani, *Nature* **2018**, *557*, 691.
[30] J. Li, S. Sanz, M. Corso, D. J. Choi, D. Peña, T. Frederiksen, J. I. Pascual, *Nat. Commun.* **2019**, *10*, 200.
[31] J. Li, N. Friedrich, N. Merino, D. G. de Oteyza, D. Peña, D. Jacob, J. I. Pascual, *Nano Lett.* **2019**, *19*, 3288.
[32] Q. Sun, X. Yao, O. Gröning, K. Eimre, C. A. Pignedoli, K. Müllen, A. Narita, R. Fasel, P. Ruffieux, *Nano Lett.* **2020**, *20*, 6429.
[33] N. Friedrich, P. Brandimarte, J. Li, S. Saito, S. Yamaguchi, I. Pozo, D. Peña, T. Frederiksen, A. Garcia-Lekue, D. Sánchez-Portal, J. I. Pascual, *Phys. Rev. Lett.* **2020**, *125*, 146801.
[34] R. E. Menchón, I. Pozo, J. Hieulle, A. Vegliante, J. Li, D. Sánchez-Portal, D. Peña, A. Garcia-Lekue, J. I. Pascual, *ACS Nano* **2022**, *16*, 14819.
[35] E. C. H. Wen, P. H. Jacobse, J. Jiang, Z. Wang, R. D. McCurdy, S. G. Louie, M. F. Crommie, F. R. Fischer, *J. Am. Chem. Soc.* **2022**, *144*, 13696.
[36] T. Wang, S. Sanz, J. Castro-Esteban, J. Lawrence, A. Berdonces-Layunta, M. S. G. Mohammed, M. Vilas-Varela, M. Corso, D. Peña, T. Frederiksen, D. G. de Oteyza, *Nano Lett.* **2022**, *22*, 164.
[37] B. Trauzettel, D. V. Bulaev, D. Loss, G. Burkard, *Nat. Phys.* **2007**, *3*, 192.
[38] G. Guo, Z. Lin, X. Li, T. Tu, *New. J. Phys.* **2009**, *11*, 123005.
[39] B. Sutherland, *Phys. Rev. B* **1986**, *34*, 5208.
[40] E. H. Lieb, *Phys. Rev. Lett.* **1989**, *62*, 1201.
[41] L. Gross, F. Mohn, N. Moll, P. Liljeroth, G. Meyer, *Science* **2009**, *325*, 1110.
[42] J. van der Lit, M. P. Boneschanscher, D. Vanmaekelbergh, M. Ijäs, A. Uppstu, M. Ervasti, A. Harju, P. Liljeroth, I. Swart, *Nat. Commun.* **2013**, *4*, 2023.
[43] L. Gross, *Nat. Chem.* **2011**, *3*, 273.
[44] S. Song, J. Su, X. Peng, X. Wu, M. Telychko, *Surf. Rev. Lett.* **2021**, *28*, 2140007.
[45] H. O. Frota, *Phys. Rev. B* **1992**, *45*, 1096.
[46] O. Újsághy, J. Kroha, L. Szunyogh, A. Zawadowski, *Phys. Rev. Lett.* **2000**, *85*, 2557.
[47] W.-H. Soe, C. Manzano, A. DeSarkar, N. Chandrasekhar, C. Joachim, *Phys. Rev. Lett.* **2009**, *102*, 176102.
[48] S. Wang, L. Talirz, C. A. Pignedoli, X. Feng, K. Müllen, R. Fasel, P. Ruffieux, *Nat. Commun.* **2016**, *7*, 11507.
[49] D. Jacob, R. Ortiz, J. Fernández-Rossier, *Phys. Rev. B* **2021**, *104*, 75404.
[50] L. Yang, C. H. Park, Y. W. Son, M. L. Cohen, S. G. Louie, *Phys. Rev. Lett.* **2007**, *99*, 186801.
[51] M. Ternes, *New. J. Phys.* **2015**, *17*, 063016.
[52] M. Pizzochero, K. Čerņevičs, G. B. Barin, S. Wang, P. Ruffieux, R. Fasel, O. V. Yazyev, *2D Mater.* **2021**, *8*, 035025.
[53] R. Ortiz, R. A. Boto, N. García-Martínez, J. C. Sancho-García, M. Melle-Franco, J. Fernández-Rossier, *Nano Lett.* **2019**, *19*, 5991.
[54] M. Golor, C. Koop, T. C. Lang, S. Wessel, M. J. Schmidt, *Phys. Rev. Lett.* **2013**, *111*, 85504.
[55] R. Ortiz, N. A. García-Martínez, J. L. Lado, J. Fernández-Rossier, *Phys. Rev. B* **2018**, *97*, 195425.
[56] M. Moro-Lagares, R. Korytár, M. Piantek, R. Robles, N. Lorente, J. I. Pascual, M. R. Ibarra, D. Serrate, *Nat. Commun.* **2019**, *10*, 2211.
[57] P. H. Jacobse, M. C. Daugherty, K. Čerņevičs, Z. Wang, R. D. McCurdy, O. V. Yazyev, F. R. Fischer, M. F. Crommie, *ACS Nano* **2023**, *17*, 24901.
[58] J. Yin, P. H. Jacobse, D. Pyle, Z. Wang, M. F. Crommie, G. Dong, *J. Am. Chem. Soc.* **2022**, *144*, 16012.
[59] T. H. Vo, M. Shekhirev, D. A. Kunkel, M. D. Morton, E. Berglund, L. Kong, P. M. Wilson, P. A. Dowben, A. Enders, A. Sinitskii, *Nat. Commun.* **2014**, *5*, 3189.
[60] L. Bartels, G. Meyer, K.-H. Rieder, *Appl. Phys. Lett.* **1997**, *71*, 213.
[61] I. Horcas, R. Fernández, J. M. Gómez-Rodríguez, J. Colchero, J. Gómez-Herrero, A. M. Baro, *Rev. Sci. Instrum.* **2007**, *78*, 13705.
[62] G. Kresse, J. Furthmüller, *Phys. Rev. B* **1996**, *54*, 11169.
[63] G. Kresse, D. Joubert, *Phys. Rev. B* **1999**, *59*, 1758.
[64] W. Kohn, L. J. Sham, *Phys. Rev.* **1965**, *140*, A1133.
[65] P. Hohenberg, W. Kohn, *Phys. Rev.* **1964**, *136*, B864.
[66] P. Giannozzi, S. Baroni, N. Bonini, M. Calandra, R. Car, C. Cavazzoni, D. Ceresoli, G. L. Chiarotti, M. Cococcioni, I. Dabo, A. Dal Corso, S. de Gironcoli, S. Fabris, G. Fratesi, R. Gebauer, U. Gerstmann, C. Gougoussis, A. Kokalj, M. Lazzeri, L. Martin-Samos, N. Marzari, F. Mauri, R. Mazzarello, S. Paolini, A. Pasquarello, L. Paulatto, C. Sbraccia, S. Scandolo, G. Sclauzero, A. P. Seitsonen, et al., *J Phys. Condens. Matter* **2009**, *21*, 395502.
[67] D. R. Hamann, *Phys. Rev. B* **2013**, *88*, 85117.
[68] A. Kokalj, *J. Mol. Graph. Model.* **1999**, *17*, 176.